# Effect of Nonlocal Transport on Heat-Wave Propagation

G. Gregori, S. H. Glenzer, J. Knight, C. Niemann, D. Price, D. H. Froula, M. J. Edwards, and R. P. J. Town
*Lawrence Livermore National Laboratory, University of California, P.O. Box 808, California 94551, USA*

A. Brantov and W. Rozmus
*Department of Physics, University of Alberta, Edmonton, Alberta, Canada T6G 2J1*

V. Yu. Bychenkov
*P. N. Lebedev Physics Institute, Russian Academy of Sciences, Moscow 117924, Russia*
(Received 27 August 2003; published 20 May 2004)

We present the first direct measurements of spatially and temporally resolved temperature and density profiles produced by nonlocal transport in a laser plasma. Absolutely calibrated measurements have been performed by Rayleigh scattering and by resolving the ion-acoustic wave spectra across the plasma volume with Thomson scattering. We find that the electron temperature and density profiles disagree with flux-limited models, but are consistent with nonlocal transport modeling.

DOI: 10.1103/PhysRevLett.92.205006 PACS numbers: 52.50.Jm, 52.35.Fp

Heat transport is a fundamental process for the laser plasma interactions in inertial confinement fusion (ICF) experiments, as well as for the correct design of ICF ignition targets [1]. Controlled energy deposition by intense lasers into a radiation cavity (hohlraum) must be properly modeled to achieve the desired symmetric convergence of implosion ICF capsules. Key issues that need to be addressed are the degree of heat transport inhibition by both nonlocal electrons and magnetic fields [2,3] together with a validation of the predictive capability of plasma conditions in gas filled hohlraums [4]. Since early experiments [5–9] and Fokker-Planck simulations [10–12], which first provided evidence of heat flux inhibition and nonlocal transport, a large theoretical effort [13–17] has been aimed to identify and model the correct mechanism for heat transport in laser-produced plasmas. In plasmas with small temperature gradients, the heat transport is described by the classical Spitzer-Härm theory [18]. This is valid when $\lambda_{ei} \ll L_t$, where $\lambda_{ei}$ is the electron-ion mean free path and $L_t$ is the spatial scale for the thermal gradients. In laser irradiated plasmas, however, the intense localized heating at the beam focus drives an expanding heat wave with steep temperature gradients. As a result, the energy flux described by the local Spitzer-Härm theory becomes invalid.

In this Letter, we report the first time-resolved observation of nonlocal transport effects on heat wave propagation in a laser-produced plasma heated for a period of time (~1 ns) much longer than the mean collision time. Spatially and temporally resolved $T_e$ and $n_e$ profiles allows a direct comparison with radiation-hydrodynamics, Fokker-Planck, and reduced nonlinear, nonlocal transport modeling. The late time evolution of the heat wave is well reproduced by Fokker-Planck simulations and by the nonlinear nonlocal reduced model, but it is not in agreement with heat flux-limited radiation-hydrodynamics predictions.

The experiments have been performed at the *Janus* laser facility at the Lawrence Livermore National Laboratory. The setup is illustrated in Fig. 1. We produce the plasma by heating a ~2 mm diameter nitrogen gas jet operating at 4.8 MPa upstream pressure with a Gaussian 1.4 ns FWHM, ~100 J driver beam at the fundamental frequency of 1064 nm ($1\omega$), with a laser intensity of $1.5 \times 10^{14}$ W/cm$^2$. The plasma is then probed perpendicular to the driver beam with a 130 ps, 0.2 J beam operating at 532 nm ($2\omega$). The probe beam was then imaged, onto a gated charge-coupled device (CCD) camera, along a 100 $\mu$m wide slit of a 0.67 m, 1200 grooves/mm spectrometer used in second order. In order to examine the heating of the plasma, the probe beam was fired at various times during the driver beam pulse.

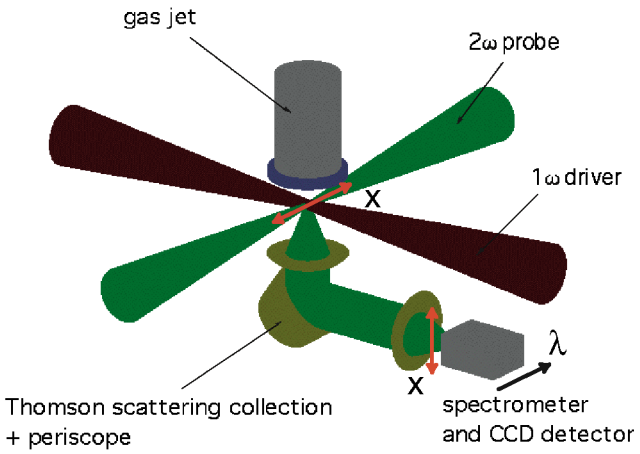


FIG. 1 (color). Experimental setup for Thomson scattering imaging. The temperature and density profiles are obtained across the ($1\omega$) driver beam. Two additional mirrors (periscope) used to flip the image are not shown in the figure.

  

Electron temperature profiles can be extracted from the Thomson scattering signal based on the wavelength separation of the ion-acoustic waves. The electron density is obtained self-consistently from absolute intensity Rayleigh scattering calibration of the instrument response [19] via the following relation: $S(k)n_e = n_R \frac{\sigma_R}{\sigma_{Th}} \frac{P_{Th} I_R}{P_R I_{Th}}$, where $S(k)$ is the frequency-integrated spectral density function (or static form factor), $n_e$ is the electron density, $n_R$ is the density of the gas used in the Rayleigh calibration, $P_{Th}$ and $P_R$ are the total Thomson and Rayleigh scattered intensities, respectively, into the detector, and $I_{Th}$ and $I_R$ are the total incident laser intensities in the Thomson and Rayleigh scattering experiments, respectively. The ratio of the Thomson cross section to the Rayleigh cross section $\sigma_R/\sigma_{Th}$ is well known for nitrogen [20].

The driver and probe beam spot sizes were also measured with Rayleigh scattering by imaging the entire beams onto the camera and by using the spectrometer in zeroth order with the entrance slit fully open. The driver beam spot at target chamber center was measured to be $\sim$320 $\mu$m, while the probe beam was $\sim$120 $\mu$m in diameter. The time resolution is determined by the probe pulse length to be 130 ps. Timing errors were estimated from the laser trigger jitter to be on the order of 150–200 ps. Spatial resolution is on the order of $\sim$50 $\mu$m. The collection lens was chosen to have a diffraction-limited spot size $\lesssim 10$ $\mu$m in order to limit effects of spatial gradients along the line of sight.

Figure 2 shows Thomson scattering (TS) spectra for three different times during the heating of a plasma. We have inferred temperature gradients from the spatially varying separation of the ion-acoustic features. The gradients are steeper at the beginning of the pulse and moderate at the end of the laser pulse. In order to test

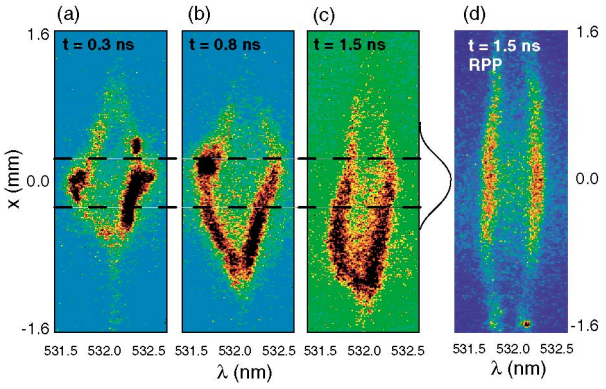


FIG. 2 (color). Spatially resolved Thomson scattering spectra. The horizontal axis is wavelength, centered at 532 nm, and the vertical axis is space along the probe beam. The probe beam propagates from the bottom to the top. (a)–(c) TS signals using an unsmoothed Gaussian ($1\omega$) driver beam, with the dashed lines indicating the area of heating. (d) TS from a RPP driver beam. Shot-to-shot accuracy in the location of $x = 0$ is $\sim$150 $\mu$m.

the uniformity of the gas jet prior to the localized driver heating, we have illuminated the jet with a smoothed driver beam. Using a $1\omega$ random phase plate (RPP) with $\sim$2 mm spot size we checked that the ion-acoustic features remain parallel and constant in intensity over the scattering volume, indicating homogeneous gas jet conditions.

The temperature profile has been extracted by fitting the whole profile with the frequency-dependent TS form factor $S(k, \omega)$. The electron density is determined self-consistently from the Rayleigh scattering calibration. In addition, the ionization state, $Z$, is calculated using an atom-averaged Thomas-Fermi model [21], giving $Z$ in the range 4–7 for $T_e$ in the range 20–350 eV. This procedure allows a direct correlation between the separation of the TS peaks and the electron temperature. Including errors in the determination of $Z$, the measured absolute temperature data are thus determined with an accuracy of 20%, and the relative $T_e$ profiles to 10% accuracy. Effects of non-Maxwellian distributions on the experimental temperatures due to the Langdon effect are estimated to be $\lesssim$5% [22].

In contrast to the case of a RPP driver beam [Fig. 2(d)], where the scattered intensity remains almost constant across the heated plasma region, in the absence of smoothing, there is an asymmetry in the intensity profiles of Figs. 2(b) and 2(c) from bottom to top. We have found that the unsmoothed high intensity pump can drive the filamentation instability with an amplitude gain length comparable to be beam waist [23]. We speculate that, when the probe beam crosses the region heated by the pump, it undergoes multiple scattering on large-amplitude long-wavelength density fluctuations produced by the filamentation instability of the pump beam. Such density fluctuations can randomize the probe beam over distances of the order of a few hundred microns (cf. Ref. [24]), and the resultant plasma induced smoothing of the Thomson probe thus reduces its intensity by spreading the beam and could account for the lower scattering signal in the top part of Figs. 2(b) and 2(c). The left-to-right asymmetry in the TS spectra is related to the presence of hot spots in the unsmoothed pump intensity distribution, which drive asymmetric transverse temperature gradients. In the analysis reported in this Letter the profiles have been obtained from the lower half of the TS images. Clearly, this introduces an overall uncertainty in the absolute electron density values by a factor of $\sim$2. However, the measured relative density profiles are determined with 20% accuracy.

Figures 3 and 4 show the electron temperature and electron density profiles for the focused driver beam, at different times during the heating cycle. The electron mean free path, using the measured values of electron temperature and density at the center of the profile ($T_e \simeq$ 300 eV, $n_e \simeq 10^{19}$ cm$^{-3}$) is $\lambda_{ei} \sim 30$ $\mu$m, comparable with the temperature gradient scale length from Fig. 3. We observe a *nonlocal* heat wave that propagates into the

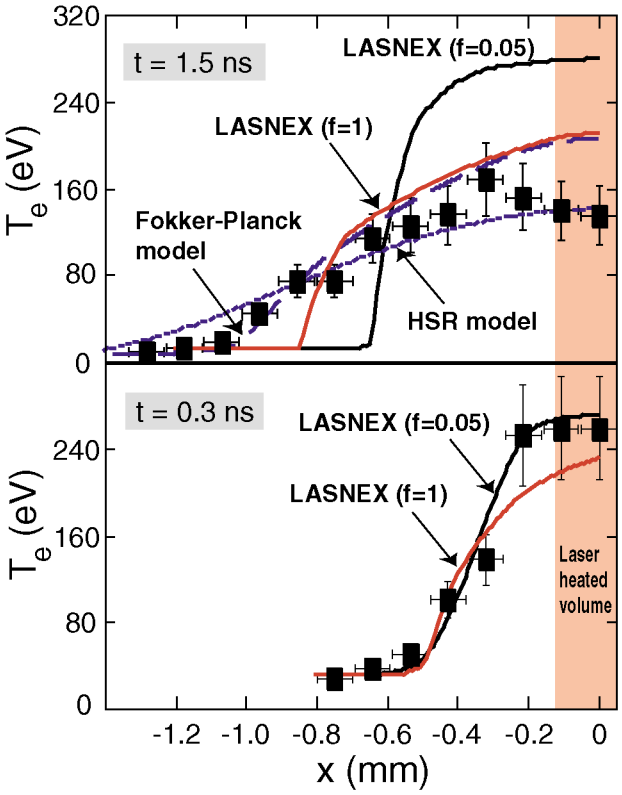


FIG. 3 (color). Electron temperature profiles at $t = 0.3$ and 1.5 ns. The shaded area corresponds to the heated area by the $1\omega$ driver beam.

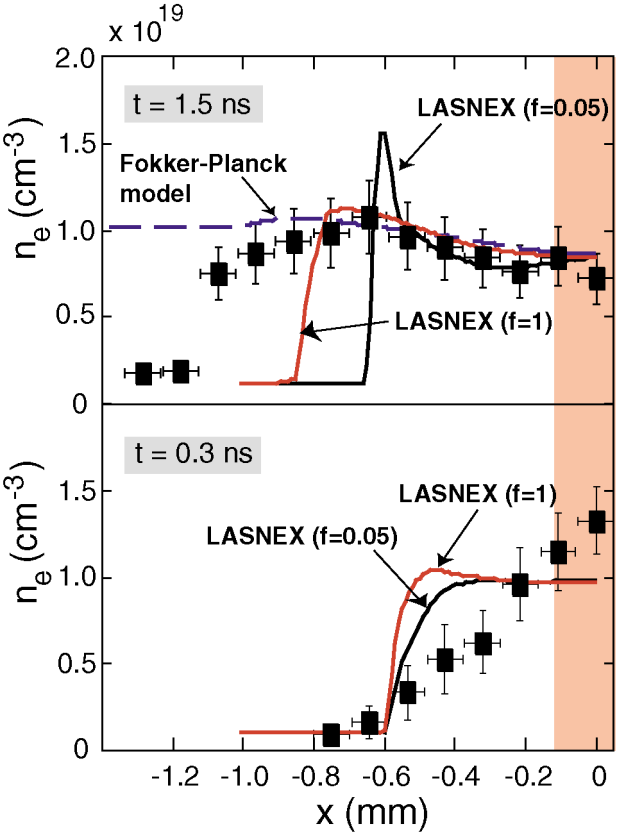


FIG. 4 (color). Electron density profiles at $t = 0.3$ and 1.5 ns. The shaded area corresponds to the heated area by the $1\omega$ driver beam.

plasma far beyond the predicted distance by flux-limited models.

The nonlocal behavior is evident from the comparison of the experimental temperature profiles with the LASNEX code [25], in which a flux-limited diffusion model was used to solve the heat flow [26], $\mathbf{q} = \min(f\mathbf{q}_{fs}, \mathbf{q}_{\mathrm{SH}})$, where $\mathbf{q}_{fs}$ is the free-streaming flux, $\mathbf{q}_{\mathrm{SH}}$ is the classical heat flow, and $f$ is a flux-limiter factor. LASNEX was used because it can also account for non-LTE (local thermodynamic equilibrium) and radiative effects, as well as hydrodynamics. Laser absorption is modeled by classical inverse bremsstrahlung, since at the operating gas jet pressure and laser intensity absorption by cluster formation is $<10\%$ [27]. Given the measured temporal and spatial intensity profiles of the driver beam, the problem has been solved in cylindrical geometry. Starting from a uniform gas density, calculated $T_e$ and $n_e$ profiles are obtained at various time intervals for two different values of the flux limiter: $f = 0.05$ and 1.

At the beginning of the heater pulse ($t = 0.3$ ns), LASNEX calculations for $f = 0.05$ agree well with the experimental temperature profiles. At these early times, the heat wave is correlated to the driver beam profile that was measured with the spatially resolved Rayleigh scattering images of the $1\omega$ beam. At later times (Fig. 3, at $t = 1.5$ ns) the measured heat wave position significantly exceeds the LASNEX prediction for both $f = 0.05$ and 1, resulting in a temperature profile that is not as steep as expected from a local theory.

We find that density profiles also reflect the propagation mechanism of the heat wave. Figure 4 shows LASNEX simulations together with measured electron density profiles at two different times. As the driver beam deposits heat in the central region of the plasma, the increased thermal pressure pushes electrons away and they bunch at the heat front. LASNEX predicts the initial stage of the hydrodynamic expansion with the steepening of the density wave up to $t \lesssim 0.5$ ns. However, at the end of the heater pulse, we see a narrow spike in the electron density profile calculated by LASNEX for $f = 0.05$ at a position corresponding to the front of the heat wave. The simulation for $f = 1$ also fails to predict the correct expansion of the density wave. Again, we interpret this as a consequence of nonlocal heat transport that results in a redistribution of the heat over a larger spatial region.

We have performed full nonlocal calculations using SPARK [28,29], a 2D code that solves the Fokker-Planck equations in the diffusion approximation. Since SPARK does not have a self-consistent ionization balance model embedded in it, we have assumed $Z = 7$ throughout the plasma, but changed laser absorption by a constant factor in order to reproduce the same absorption as calculated by LASNEX and in agreement with the experiment. At

$t = 1.5$ ns, we see from the temperature plot of Fig. 3 that SPARK reproduces well the measured profile, even far from the central region of the plasma. The SPARK density profile does not show a pressure spike and is flat over the entire region in agreement with the measured one for $|x| \lesssim 1$ mm, but dramatically different at the edges, probably because of the constant $Z$ constraint in the code.

Presently, Fokker-Planck solvers have not been incorporated into 2D or 3D radiative hydrodynamic codes for a complete nonlocal plasma simulation predictive capability. More computationally efficient reduced models that can be embedded into fluid codes and preserve nonlocality of electron transport have been developed. We have tested a nonlinear nonlocal model, the hot spot relaxation (HSR) [30], that in the limit of small perturbations reproduces the exact linear nonlocal hydrodynamics [16]. The experimental temperature profile, $T_e(x)$, at the peak of the heating cycle is used as the initial condition for the HSR problem:

$$\frac{\partial T_e}{\partial t} - \frac{2}{3n_e}\frac{\partial q(x,t)}{\partial x} = 0, \tag{1}$$

where the electron heat flux $q(x, t)$ is defined as follows:

$$q(x) = \int_{-\infty}^{\infty} q_{\mathrm{SH}}(x')G(x,x')\,dx', \tag{2}$$

with $q_{\mathrm{SH}}(x) = -\kappa_0 \partial T_e/\partial t$ the Spitzer-Härm heat flux, $\kappa_0 = \frac{128}{3\pi}\gamma_\kappa n_e v_{Te}\lambda_{ei}$, $\gamma_\kappa = \frac{0.24+Z}{4.2+Z}$, where the electron-ion mean free path is $\lambda_{ei}(T_e) = 3T_e^2/4\sqrt{2\pi}Zn_e e^4\Lambda$ ($\Lambda$ is the Coulomb logarithm). The essential details of the transport are included in the kernel $G(x, x')$. Spitzer-Härm transport is reproduced by setting $G(x, x') = \delta(x - x')$ in Eq. (2). As a nonlocal transport model we have used

$$G(x,x') = \frac{\xi(\eta(x-x',x'))}{\pi a \lambda_e(x')}, \qquad \xi(\eta) = \int_0^\infty \frac{dp\cos\eta p}{1+p^{0.9}}, \tag{3}$$

where $\eta = |x - x'|/a\lambda_e(x')$. This form of the nonlocal kernel is a generalization of the linear nonlocal theory results for the thermal transport conductivity [16] in the Fourier space ($k \rightarrow x - x'$):

$$\kappa(k) = \frac{\kappa_0}{1 + (ak\lambda_e)^{0.9}}, \qquad \lambda_e = \sqrt{Z}\,\lambda_{ei}, \qquad k\lambda_{ei} \lesssim 1, \tag{4}$$

where $a = 10(Z + 5)/(Z + 12)$. However, we also account for the local variations of $n_e(x')$, $T_e(x')$ in $\lambda_e$. This approach indeed shows good agreement with the measured temperature profiles in Fig. 3.

In summary, we have presented the first measurement of nonlocal effects on heat wave propagation in a laser-produced plasma. Our temperature and density profiles have been directly applied to test theoretical transport models. Calculations based on classical local hydrodynamics, Fokker-Planck codes, and semianalytical solutions of the nonlocal transport equations have been compared with the heat wave propagation showing the importance of kinetic nonlocal effects in electron transport, and finding better qualitative agreement with the latter two models. These results are important to understand the energy deposition mechanisms in laser-produced plasmas, in particular, for the modeling of hohlraum targets in ICF research.

This work was performed under the auspices of the U.S. Department of Energy by the University of California Lawrence Livermore National Laboratory under Contract No. W-7405-ENG-48. The SPARK code was developed at the University of Rochester's Laboratory for Laser Energetics supported by the U.S. DOE under Contract No. DE-FC03-92SF19460.

[1] J. D. Lindl, Phys. Plasmas **2**, 3933 (1995).
[2] D. S. Montgomery *et al.*, Phys. Rev. Lett. **73**, 2055 (1994).
[3] C. A. Back *et al.*, Phys. Rev. Lett. **77**, 4350 (1996).
[4] S. H. Glenzer *et al.*, Phys. Plasmas **6**, 2117 (1999).
[5] D. R. Gray and J. D. Kilkenny, Plasma Phys. **22**, 81 (1980).
[6] P. Alaterre *et al.*, Phys. Rev. A **32**, 324 (1985).
[7] J. H. Rogers *et al.*, Phys. Fluids B **1**, 741 (1989).
[8] A. Djaoui and A. A. Offenberger, Phys. Rev. E **50**, 4961 (1994).
[9] T. Ditmire *et al.*, Phys. Rev. Lett. **80**, 720 (1998).
[10] A. R. Bell *et al.*, Phys. Rev. Lett. **46**, 243 (1981).
[11] R. J. Mason, Phys. Rev. Lett. **47**, 652 (1981).
[12] J.-P. Matte and J. Virmont, Phys. Rev. Lett. **49**, 1936 (1982).
[13] J. F. Luciani, P. Mora, and J. Virmont, Phys. Rev. Lett. **51**, 1664 (1983).
[14] J. R. Albritton *et al.*, Phys. Rev. Lett. **57**, 1887 (1986).
[15] E. M. Epperlein and R. W. Short, Phys. Fluids B **3**, 3092 (1991).
[16] V. Y. Bychenkov *et al.*, Phys. Rev. Lett. **75**, 4405 (1995).
[17] A. V. Brantov *et al.*, Phys. Plasmas **5**, 2742 (1998).
[18] L. Spitzer and R. Härm, Phys. Rev. **89**, 977 (1953).
[19] A. Gawron *et al.*, Phys. Rev. A **38**, 4737 (1988).
[20] H. J. Kunze, in *Plasma Diagnostics*, edited by W. Lochte-Holgreven (John Wiley & Sons, New York, 1995).
[21] D. Salzmann, *Atomic Processes in Hot Plasmas* (Oxford University Press, Oxford, U.K., 1998).
[22] S. H. Glenzer *et al.*, J. Quant. Spectrosc. Radiat. Transfer **65**, 253 (2000).
[23] V. Y. Bychenkov *et al.*, Phys. Plasmas **7**, 1511 (2000).
[24] V. Malka *et al.*, Phys. Rev. Lett. **90**, 075002 (2003).
[25] G. B. Zimmerman and W. L. Kruer, Comments Plasma Phys. Control. Fusion **2**, 51 (1975).
[26] R. C. Malone *et al.*, Phys. Rev. Lett. **34**, 721 (1975).
[27] T. Ditmire *et al.*, Phys. Rev. Lett. **78**, 3121 (1997).
[28] E. M. Epperlein, G. J. Rickard, and A. R. Bell, Comput. Phys. Commun. **52**, 7 (1988).
[29] R. P. J. Town, A. R. Bell, and S. J. Rose, Phys. Rev. E **50**, 1413 (1994).
[30] O. V. Batishchev *et al.*, Phys. Plasmas **9**, 2302 (2002).